Full length article

Gas-filled protein nanostructures as cavitation nuclei for molecule-specific sonodynamic therapy

Lin Song [a,b,1], Xuandi Hou [a,1], Kin Fung Wong [a], Yaoheng Yang [a], Zhihai Qiu [a], Yong Wu [a], Shang Hou [c], Chunlong Fei [c], Jinghui Guo [a], Lei Sun [a,*]

[a] Department of Biomedical Engineering, The Hong Kong Polytechnic University, Hung Hom Room ST409, Hong Kong SAR, PR China
[b] School of Basic Medicine, Qingdao University, Qingdao, PR China
[c] School of Microelectronics, Xidian University, Xi'an, PR China

A B S T R A C T

Sonodynamic therapy (SDT) is a promising alternative for cancer therapy, understood to exert cytotoxicity through cavitation and subsequent production of large amounts of reactive oxygen species (ROS). Gas-filled protein nanostructures (gas vesicles or GVs) produced by cyanobacteria have a hollow structure similar to microbubbles and have demonstrated comparable enhancement of ultrasound imaging contrast. We thus hypothesized that GVs may act as stable nuclei for inertial cavitation to enhance SDT with improved enhanced permeability and retention (EPR) effects due to their nanometer scale. The function of GVs to mediate cavitation, ROS production, and cell-targeted toxicity under SDT was determined. In solution, we found that GVs successfully increased cavitation and enhanced ROS production in a dose- and time-dependent manner. Then, GV surfaces were modified (FGVs) to specifically target CD44+ cells and accumulate preferentially at the tumor site. In vitro sonodynamic therapy (SDT) showed ROS production and tumor cell toxicity substantially elevated in the presence of FGVs, and the addition of FGVs was found to enhance cavitation and subsequently inhibit tumor growth and exert greater damage to tumors under SDT in vivo. Our results thus demonstrate that FGVs can function as stable, nanosized, nuclei for spatially accurate and cell-targeted SDT.

Statement of significance

The initiation of inertial cavitation is critical for ROS generation and subsequent cellular toxicity in SDT. Thus, precise control of the occurrence of cavitation is a key factor in increasing SDT's therapeutic efficacy. We explored nanometer-sized gas vesicles (GVs) as a new class of cavitation nuclei for molecule-specific sonodynamic therapy. Our results showed that GV-mediated SDT treatment enabled targeted disruption of specific cells expressing a known surface marker within the area of insonation, providing a spatially specific and targeted SDT treatment.

1. Introduction

In the past several decades, the first-line treatments for most cancers have been surgical resection, chemotherapy, and radiotherapy, and they have provided significant benefits to patients [1–4]. Simultaneously, significant attention has been paid to the development of new, more efficient therapeutic modalities. Sonodynamic therapy (SDT) has emerged as a promising non-invasive therapeutic modality [5–8]. SDT combines low-intensity ultrasound and a 'sonosensitizer' to generate cytotoxicity in tumors [9–11]. It has the advantage of being able to target tumors with high spatial resolution since ultrasound can be focused on a single point deep within tissues in three dimensions while leaving normal tissue undamaged [6,12]. Such precise disruption of selected tissues using focused ultrasound provides an advantage in developing treatments for deep-seated tumors [5,10,12,13].

Ultrasound enables SDT by inducing inertial cavitation, which is the process of nucleation, growth, and implosive collapse of bub-

* Corresponding author.
  E-mail address: lei.sun@polyu.edu.hk (L. Sun).
  [1] These authors contributed equally to this work.

bles during which extreme temperatures and pressures are generated [9,10]. It has been suggested that inertial cavitation events during SDT can generate light through sonoluminescence and potentially activate sonosensitizers to generate ROS [7,9,10]. Concurrently, the localized high temperatures generated by inertial cavitation are also believed to generate free radicals which then directly react with endogenous substances to generate ROS [6,7,9]. Thus, being able to accurately modulate and enhance inertial cavitation is critical for precise targeting as well as ROS generation and the subsequent therapeutic efficacy. *In vivo* cavitation nucleation thresholds are usually high (5–7 MPa) due to a lack of naturally occurring nuclei, and targeted contrast agents like microbubbles (MBs) are usually added to lower the nucleation threshold, making cavitation more specific and easier to sustain and control [14–18]. However, the *in vivo* dwell time of microbubbles is limited due to their inherent instability and their micron size preventing them from extravasating to tumor sites, compromising their therapeutic capability [14,19–21].

Gas-filled protein nanostructures called gas vesicles (GVs) have recently been demonstrated to enhance ultrasound imaging contrast, comparable to MBs [22–28]. Unlike microbubbles, GVs are biogenic nanobubbles derived from buoyant cyanobacteria, composed of a hydrophobic interior protein layer and a hydrophilic exterior protein layer [23,29–31]. This special structure allows GVs to exclude water but allow gas exchange through the protein shell, endowing them with robust physical stability [24,30]. To facilitate GVs to escape rapid clearance by the reticuloendothelial system after tail injection, surface modifications were made for GVs using polyethylene glycol (PEG) and hyaluronic acid (HA). Our lab has recently shown that these functionalized GVs (FGVs) were capable of extravasating into deep tumor regions and target CD44+ tumor cells specifically *in vivo* [32].

Given the hollow structure of GVs and their MB-like ultrasound contrast enhancement capability, we hypothesized that GVs could serve as ultrasound-responsive cavitation nuclei to facilitate cavitation during SDT. Furthermore, functionalized GVs could improve SDT's potency by allowing the targeting of a specific cell population. However, whether or not GVs could function as ultrasound-responsive cavitation nuclei to enable targeted disruption of tumors and SDT enhancement remains unknown. Here, we report that GVs' presence during SDT enhanced ROS production, cell apoptosis *in vitro* as well as severe tissue damage *in vivo*. We provide evidence for GVs being an efficient and simple way to enhance the efficiency of targeted SDT against tumors.

2. Materials and methods

2.1. Reagents

Dulbecco's Modified Eagle Medium (DMEM), Fetal bovine serum (FBS), trypsin-EDTA (0.25%) solution, and Penicillin-streptomycin solution were purchased from Life Technologies (Carlsbad, CA, USA). Annexin V-FITC/PI Apoptosis Detection Kit and 2′,7′-dichlorodihydrofluorescein-diacetate (H2DCF-DA) were purchased from Invitrogen (Carlsbad, CA, USA). CCK-8 assay kit was purchased from Sangon Biotech (Shanghai, China). 1-ethyl-3-(3-(dimethylamino)propyl) carbodiimide (EDC), and Nhydroxysuccinimide (NHS) was obtained from J&K company (Beijing, China). ICG-Sulfo-Osu (ICG) was purchased from Dojindo molecular technologies (Tokyo, Japan). Methoxypolyethylene glycol amine (PEG-amine, molecular weight=5 kDa) was purchased from Shanghai Seebio Biotech (Shanghai, China). Sodium hyaluronic acid (HA, molecular weight= 234 kDa) was obtained from Lifecore Biomedical (Chaska, MN). Protoporphyrin IX disodium salt was purchased from Sigma chemical company (St. Louis, MO, USA).

2.2. Preparation, functionalization, and characterization of GVs

Anabaena flos-aquae GVs and functionalized GVs were produced and manufactured as described previously [32]. Briefly, GVs were isolated and purified through tonic cell lysis of *Anabaena flos-aquae*, washed three times by centrifugation, and stored in phosphate-buffered saline (PBS) at 4 °C. The concentration of GVs was estimated using a literature-based formula (450 nM per OD_{500}). Briefly, GVs concentration was determined by optical density method characterized by 500 nm wavelength light (OD500) by UV-Visible spectrophotometer and calculated to molar concentration with the ratio of 450 pM/OD500. Functionalized GVs were made to facilitate tumor targetability and accumulation especially *in vivo*. For functionalized GVs (FGVs) synthesis, polyethylene glycol (PEG) and hyaluronic acid (HA) were linked to the GVs' s protein shells by covalent conjugation [33–36]. Firstly, EDC (3.37 mg) and NHS (2 mg) were added to HA solution (10 mg) in PBS (pH = 7.4), mixed with 1 mL of GVs (5 nM) dissolved in PBS. The reaction mixture was stirred for 24 h at 4 °C. Then, PEG was chemically conjugated to the HA-GVs conjugate through amide formation in the presence of EDC and NHS. The HA-GVs conjugate mixed with EDC (3.37 mg), NHS (2 mg) in PBS, and PEG-amine (73.5 mg), the mixture was stirred for 24 h in an ice bath. HA derivative bearing five PEG molecules per 100 sugar residues of HA was coated on GVs. The resulting solution was then centrifuged and washed 4 times with PBS. To trace functionalized GVs by fluorescent signals, GVs were also labeled with a NIR dye, Indocyanine green (ICG). Briefly, EDC and NHS were added to ICG solution in PBS (pH = 7.4). After 30 min incubation at room temperature, the solution was added to pure GVs solution (molar ratio: ICG/GVs=1000/1).

To characterize GVs, size distribution and zeta potentials were determined by laser light scattering using a 90 Plus instrument (Brookhaven, Holtsville, NY, USA) at a fixed angle of 90° and a temperature of 25 °C. The size and morphology of GVs were determined by Transmission Electron Microscopy (TEM) with an operating voltage of 200 kV. Samples of GVs (OD 0.1) were deposited on a carbon-coated formvar grid. HA and PEG conjugation on GVs were confirmed by FTIR spectroscopy(ALPHA-T, Bruker, Germany). The prepared samples were loaded on the machine detector, and the Fourier transform infrared (FTIR) spectra were collected in the 4000–650 cm^{-1} range, with a resolution of 4 cm^{-1} at room temperature. Fluorescence spectra of FGV and ICG-FGV were performed on spectrofluorimeter (Edinburgh Instruments, Britain) at 25 °C. The ICG, ICG-GVs, and GVs were suspended in DI H_2O in a final volume of 2 mL, and the relevant emission spectra were measured using an excitation wavelength of 780 nm.

2.3. Ultrasonic characterization and system setup for SDT

For SDT experiments, a 1 MHz planar ultrasonic transducer with a diameter of 13 mm (A303S, Olympus, Tokyo, Japan) was used for sonication in this study. Function generators (Tektronix AFG3251, Agilent Technologies, USA) and a power amplifier (A075; Electronics & Innovation Ltd, USA) were used to generate high-intensity ultrasonic pulses. Cell culture dishes were placed on top of the transducer, coupled with a layer of ultrasound gel at 25 °C. Acoustic pressure distribution was characterized by a hydrophone (HNP-1000, Onda, Sunnyvale, CA, USA; pre-amplifier: AH-2010, Onda, Sunnyvale, CA, USA). The solution and the *in vitro* cell culture were sonicated with the same parameters, with the bursts of pulses at a duty cycle of 50% and pulse repetition frequency (PRF) of 1 kHz, with a pulse on/off intervals of 1 s/1.5 s to decrease heat accumulation. The spatial and temporal peak rarefactional pressure (PRP) was measured to be 0.4 MPa and an overall sonication duration was 5 min. The temperature increase was less than 1.5 °C,

as monitored with a thermometer (Checktemp®1 HI98509, Hanna Instruments, Woonsocket, RI, USA).

2.4. Acoustic cavitation detection

To evaluate GV-mediated cavitation, an experimental test platform was built as shown in Fig. 3a, b following well-established Rayleigh–Plesset equations which describe the dynamical nonlinear response of bubbles exposed to ultrasound [16]. A tank filled with deionized, degassed water was prepared to facilitate ultrasonic signal transmission. The single element 1 MHz flat transducer was installed on a three-axis translation stage and submerged in the water tank, emitting ultrasound to the GVs. To receive the signal from the GVs and avoid the signal from incident acoustic wave, a hydrophone was positioned at an angle of 90° to the emitting transducer. A rectangular 3% agarose chamber with 5 mm wall thickness, whose acoustic impedance was similar to the water to minimize reflection and energy loss, was aligned at the center of the GV container.

Bursts of pulses for SDT were generated to drive the emitting transducer. The received signals from the hydrophone were captured by a 12-bit digitizer board (GaGe CSE1222, Dynamic Signals LLC, Lockport, IL, USA) at a 200 MHz sampling rate. Using MATLAB (Mathworks, USA), 250 µs of waveform containing cavitation signal by a single burst was processed by fast Fourier transform (FFT) and resulting spectra of 36 bursts, from 9 samples (4 bursts each) were averaged to obtain the frequency-domain characteristics. To quantify the characteristic broadband signal from inertial cavitation, the 36 frequency spectra, without averaging, were smoothed using MATLAB to remove the fundamental and harmonic peaks. Spectrum of a blank recording (without sonication) was subtracted from each smoothed spectrum, the resulting spectra were then integrated from 0 MHz to 3.5 MHz, then divided by 3.5 MHz, to obtain the quantified broadband signal.

2.5. Cell culture and cellular attachment experiments

Squamous cell carcinoma (SCC-7 cells) was purchased from the Cell Bank of Type Culture Collection of the Chinese Academy of Sciences (Shanghai, China). SCC-7 cells were maintained in Dulbecco's modified Eagle's medium (DMEM, Life Technologies, Carlsbad, CA, USA) supplemented with 10% fetal bovine serum (FBS, Life Technologies), 100 units/ml penicillin, and 100 µg/ml streptomycin. Cells were maintained at 37 °C in a humidified chamber containing 95% air and 5% CO_2. Cells at a confluence of 80% were digested with 0.25% trypsin for subculture. Functionalized GVs were used for *in vitro* experiments. Cells were divided into eight treatment groups: (1) PBS(US-), (2) FGVs(US-), (3) PpIX(US-), (4) PpIX+FGVs(US-), (5) PBS(US+), (6) FGVs(US+), (7) SDT, (8) SDT+FGVs. Protoporphyrin IX (PpIX) disodium salt was purchased from Sigma-Aldrich, reconstituted in 100% DMSO (Sigma-Aldrich, St. Louis, MO, USA) to 1 mM and stored at 4 °C. For PpIX treatment, cells were incubated with PpIX (1 µM) for a 1 h drug-loading time in DMEM medium supplemented with 10% FBS. The concentration of GVs used in cell culture was 2 nM. After ultrasound treatment, cells were cultured in a fresh medium for 4 h and then prepared for different analyses.

For cell targeting experiments, SCC-7 cells seeded in confocal dishes were incubated with ICG-labeled GVs at 37 °C for 4 h, washed thoroughly with cold PBS, fixed in cold ethanol for 15 min at −20 °C, mounted with mounting medium containing DAPI. Cell internalization of ICG labeled GVs was observed by a fluorescent microscope (Olympus, USA) and the excitation and emission wavelengths were set at 780 nm and 800 nm for ICG, respectively.

2.6. ROS detection in solution and in vitro

For singlet oxygen detection in the solution, Singlet Oxygen Sensor Green (SOSG) solution (10 µM) in degassed PBS (pH 7.4) was added into PpIX (1 µM) with or without GVs (2 nM). The solution was exposed to ultrasound in the dark. The fluorescence intensity of SOSG was measured by a microplate reader at an excitation wavelength of 488 nm and an emission wavelength of 530 nm. Intracellular ROS production was measured using DCFH-DA(Sigma-Aldrich). Briefly, 10 µM DCFH-DA diluted with PBS were added to SCC-7 cells at 37 °C for 20 min. Cells were then washed with PBS three times. Labeled cells were observed by fluorescent microscopy with X20 (Nikon, Tokyo, Japan).

2.7. Cell viability, apoptosis detection

Cell viability was determined using a Cell Counting Kit-8 (Sigma-Aldrich) according to the manufacturer's instructions. Briefly, cells were plated at a density of 5×10^3 cells per well in a 96-well plate and incubated in 100 µl culture medium for 24 h. After SDT treatment, cytotoxicity was determined by adding 10 µl CCK-8 reagent per well for 1 h at 37 °C in 5% CO_2. The absorbance of the treated samples against a blank control was measured at 450 nm by a microplate reader (Bio-Tek Instrument Inc, USA). The relative viability of treated cells was determined by comparing them with the control group. Cell apoptosis was tested by Alexa Fluor 488 Annexin V/Dead Cell Apoptosis Kit (Thermo Fisher Scientific) according to the manufacturer's instructions. Briefly, cells were seeded at a density of 5×10^5 cells in 6 cm dishes and treated with SDT. After different kinds of treatments, cells were collected and incubated with 5 µl annexin V conjugate and 1 µl PI working solution at room temperature for 15 min. Cells were then analyzed by FACS Calibur flow cytometer (Becton-Dickinson, USA). The percentage of apoptosis and necrosis were analyzed by BD Accuri C6 Software (Becton-Dickinson, USA).

2.8. In vivo SDT

All procedures using laboratory animals were approved by the Department of Health, The Government of the Hong Kong Special Administrative Region, and the Hong Kong Polytechnic University Animal Subjects Ethics Sub-committee. 5–7 weeks female athymic nude mice weighing 16–18 g were supplied by the Animal Resource center of the University of Hong Kong. The mice were acclimated to the room for one week after arrival and were maintained on a normal 12 h light-dark cycle. The mice were housed in conventional cages (6 animals/cage) with free access to a standard pellet diet and water in specific pathogen-free conditions with 24 ± 2 °C temperature, 60–70% relative humidity. Standard wood chips for mice were used as bedding material. After 1 week's acclamation, 4×10^6 squamous cell carcinoma cell lines (SCC-7) in PBS (80 µl) were injected into the rear dorsal flank of nude mice by subcutaneous injection. Tumor formation occurred approximately two weeks after cell implantation and experiments were begun when tumor volume reached ~ 150 mm^3.

For *in vivo* SDT, PpIX was administrated at the dose of 5 mg/kg through pure topical injection around the tumor 1 h before SDT treatment. Functionalized GVs were used for *in vivo* experiments and were injected into mice in two ways: intravenously and intratumorally. The mice were randomly subdivided into six groups, including (1) PBS (US-), (2) PBS (US+), (3) FGVs (US+), (4) SDT, (5) SDT+FGVs(*i.v.*), (6) SDT+FGVs(*i.t.*). For ultrasound treatment, tumors were exposed to the ultrasound transducer with a peak rarefactional pressure (PRP) of 0.4 MPa for 5 min. The tumor size and body weight of each mouse were measured every 3 days following the treatment. Subcutaneous tumor volume was estimated

by the following formula: Tumor volume ≈ largest diameter × smallest diameter^2/2. All mice were sacrificed on day 15 and tumor tissues were collected and fixed in 4% paraformaldehyde for 24 h, processed through conventional histological techniques, and stained with hematoxylin and eosin (H&E). Images were captured by a Nikon optical microscope (Tokyo, Japan) and analyzed using Nikon NIS-Elements software.

2.9. Statistical analysis

Statistical analysis was performed with GraphPad Prism software. Image J, Photoshop CS, and Illustrator CS software were used for image processing following the general guidelines. All data, expressed as mean ± SD, were analyzed with a two-tailed student's *t*-test or by one-way ANOVA. *P*-values < 0.05 were considered statistically significant.
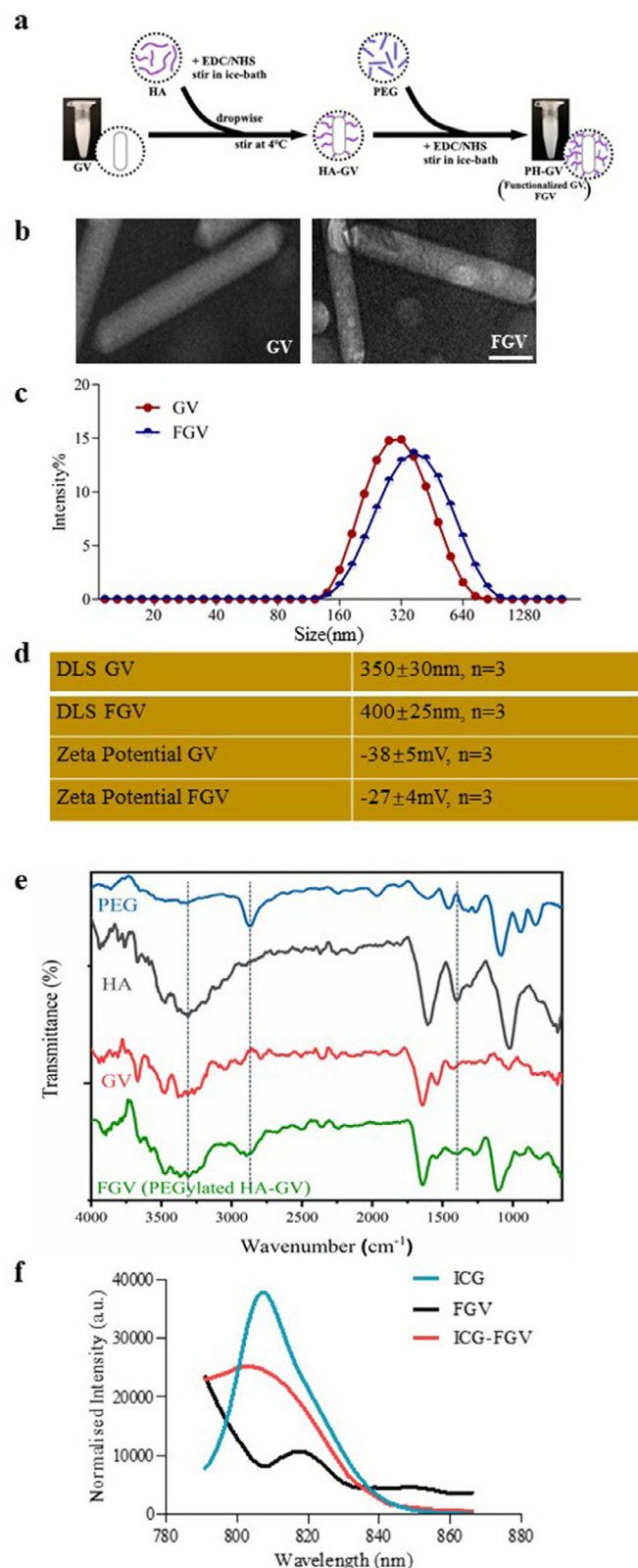
3. Results

3.1. GVs characterization

The GVs and functionalized GVs (FGVs) we prepared were visible at 1 nM in solution as a white liquid (Fig. 1a). A TEM micrograph revealed the GVs groups to be of standard cone-tipped cylinder morphology (Fig. 1b). Particle characterization revealed that the two GVs types did not differ significantly from each other in physical characteristics. The mean diameters of GVs and FGVs as determined by dynamic light scattering (DLS) were 350 ± 30 nm and 400 ± 25 nm, respectively (Fig. 1c,d) with negative zeta potentials of -38 ± 5 mV and -27 ± 4 mV, respectively (Fig. 1d). FTIR spectroscopy was performed to confirm the presence of functional groups PEG and HA over the surface of GVs. The characteristic peaks of PEG-HA-GVs can be ascribed to 1404 cm^{-1} for the C-H bending, and 3318 cm^{-1} for O-H stretching vibrations, which confirming the successful HA modification, and 2870 cm^{-1} for C-H stretching vibrations indicating the successful PEG modification. In contrast, no corresponding peaks existed in GVs alone group at the same areas. Thus, the data indicated that the PEG and HA were successfully loaded with our GVs. The fluorescence spectrum of ICG-FGV in Fig. 1f displayed a characteristic peak of ICG in the ICG-FGV sample, but not in the pure FGV sample, this indicated that ICG was successfully attached with FGV.

3.2. SDT setup and cavitation detection

The schematic diagram of the SDT setup is shown in Fig. 2a. We monitored the temperature change of ultrasound gel during the experiment and the data is shown in Fig. 2b. The temperature of the gel increased by less than 1.2 °C throughout the whole experiment (5 min' sonication). Peak rarefactional pressure (PRP) measured by a hydrophone is shown in Fig. 2c and d. It is shown that acoustic output within the central zone of approximately 15 mm in diameter is generally uniform, where PRP indicated throughout the whole article is located.

To test whether GVs could facilitate cavitation, GVs were sonicated under different PRPs. We performed cavitation detection under the same acoustic settings as in the SDT experiment. Block diagram and a top view of setup for cavitation detection were shown in Fig. 3a and b. Representative scattered signals in the time-domain (Fig. 3c,d) showed a dose-dependent increase in amplitude from both GVs and PBS. GVs showed slightly greater response under 0.1 MPa (Fig. 3c–e) which the difference significantly enlarged under 0.4 MPa (Fig. 3d–f). In the frequency-domain plot (Fig. 3g,h), under 0.1 MPa (Fig. 3g), strong fundamental (1 MHz) and notable harmonic (2, 4, and 5 MHz) could be observed from both GVs and

DLS GV	350±30nm, n=3
DLS FGV	400±25nm, n=3
Zeta Potential GV	-38±5mV, n=3
Zeta Potential FGV	-27±4mV, n=3

Fig. 1. GVs Characterization. (a) The schematic diagram for surface modification of GVs. (b) TEM micrograph of GVs and functionalized GVs. Scale bar represents 100 nm. (c) Dynamic light scattering size distribution profiles are for GVs and FGVs. (d) Summary data of size distribution profiles and zeta potentials analysis of GVs and functionalized GVs in water at pH 7.4. Data represent the mean ± SD from 3 independent experiments. (e) FTIR spectra of GV, PEG, HA and FGV. Results are representative of at least three independent experiments. (f) Fluorescence emission spectra of FGV and ICG-FGV with the relevant emission spectra measured at an excitation wavelength of 780 nm. Results are representative of at least three independent experiments.
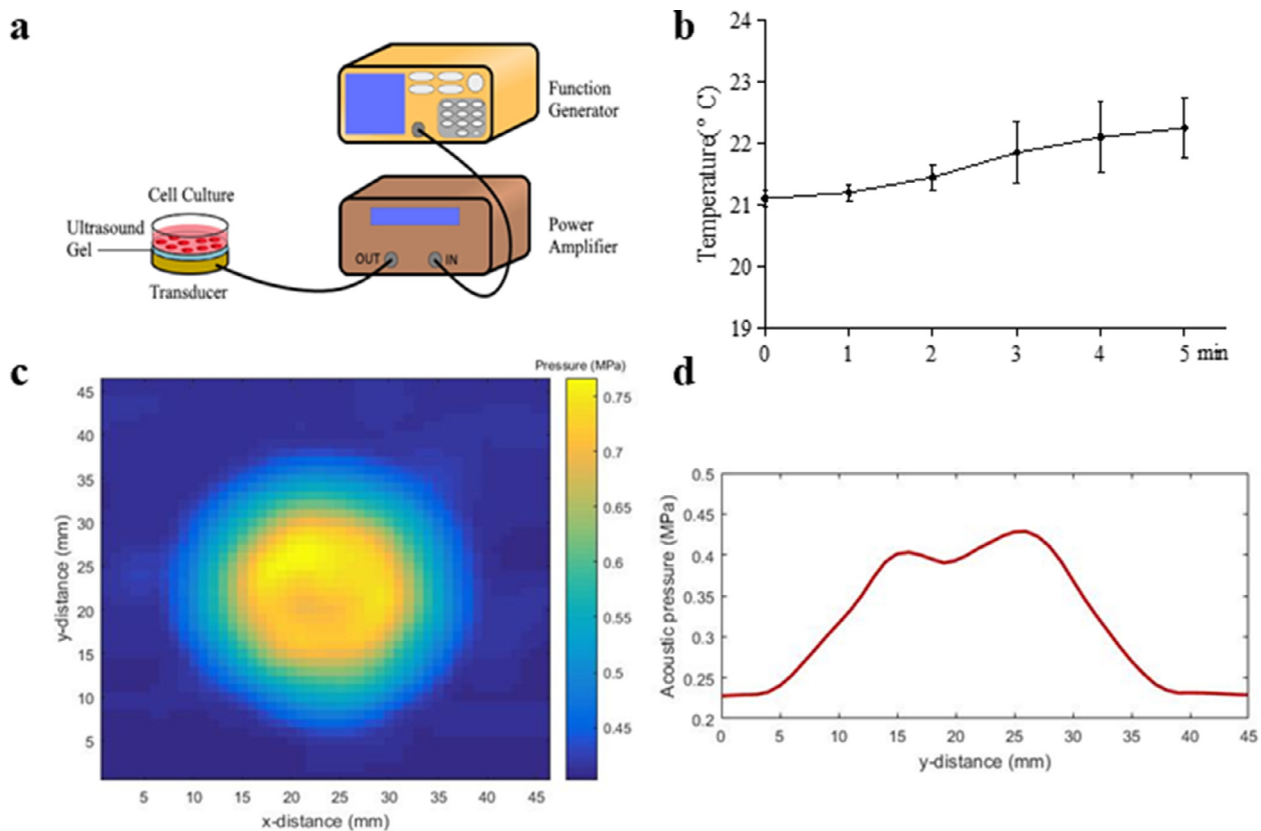
Fig. 2. Characterization of SDT system and transducer. (a) Schematic diagram of setup for SDT experiment. (b) The temperature change of ultrasound gel was assessed with a one-minute interval for ten minutes under the same setting as the SDT experiment. Data represent the mean ± SD based on 3 independent experiments. (c) 2D acoustic profile of the emitting transducer at the parallel surface of distance 2.5 cm. (d) 1D acoustic profile along the centerline (x = 22 mm).

PBS, which those from GVs were, in general, slightly greater in amplitude; when the PRP increased to 0.4 MPa (Fig. 3h), similar pattern, strong fundamental (1 MHz) and harmonic (2–5 MHz) peaks were observed from both GVs and PBS. It can be observed that both amplitude and area under the curve of the peaks from GVs are greater than those from PBS. The two observations suggest the occurrence of enhanced stable cavitation with the presence of GVs in both cases. It is also worthies notice that under 0.4 MPa, from 0 to 3 MHz, a broadband signal could be observed overlaying the fundamental and harmonic frequencies for GVs, indicating the co-occurrence of both stable cavitation and inertial cavitation, which could not be observed from PBS. Taken together, the data showed that GVs could serve as artificial nuclei for ultrasound-induced inertial cavitation under our acoustic settings for SDT. Since GVs are biologically prepared particles, to quantitatively ensure the heterogeneity is insignificant, we extracted and quantified broadband signal (Fig. 3i), all samples except PBS under 0.4 MPa showing around 0.3 dB error (around 1.4 dB for PBS under 0.4 MPa), indicating good repeatability of our testing.

3.3. GVs mediated ROS production in the solution

For SDT experiments, PpIX(1 μM) was used as sonosensitizer and the pressure of ultrasound used during SDT is 0.4 MPa. To determine whether there was direct ROS production during the interaction of GVs with ultrasound, we used the fluorescent probe SOSG (10 μM) to detect the production of singlet oxygen in a cell-free system. There were minimal fluorescent signals without ultrasound, but large increases in SOSG fluorescence were observed upon sonication in the GVs (US+) group, SDT group, and SDT+GVs group, indicating singlet oxygen production (Fig. 4a). The SDT+GVs

group showed the highest singlet oxygen production and was significantly higher than SDT alone. This indicates a synergistic effect of GVs, leading to enhanced ROS production during SDT. We also determined singlet oxygen production in the SDT group as ultrasonic exposure time increased and found that the SDT+GVs showed higher fluorescence over time (Fig. 4b). Beside, increasing GV concentration during SDT resulted in greater ROS production, showing a dose-dependence relationship (Fig. 4c). Thus, we found that the addition of GVs during SDT produced significantly greater ROS in solution and that these effects could be controlled by changing sonication time or the dose of GVs.

3.4. GVs mediated ROS production in vitro

To enhance the GVs' targeting ability and their tumor site accumulation, FGVs were used in our following *in vitro* and *in vivo* experiments. As we have demonstrated before, GVs surface-modified with HA can target CD44$^+$ tumor cells, extravasate into tumor regions and accumulate in the tumor site after intravenous injection [32]. SCC-7 cells were incubated with ICG-FGVs for 4 h and the image showed that FGVs could successfully locate around and inside SCC7 cells (Fig. 5a,b). We then investigated whether the presence of FGVs during SDT could enhance intracellular ROS production *in vitro* by monitoring DCHF-DA fluorescence. ROS production increased in the FGVs(US+) and SDT groups compared to PBS when sonicated, but the SDT+FGVs group consistently showed the highest ROS production, significantly higher than the SDT-only group (Fig. 5c,d). Little signal was observed among those groups without ultrasound irradiation. These data show that adding FGVs could significantly enhance intracellular ROS production for CD44$^+$ tumor cells during SDT *in vitro*.
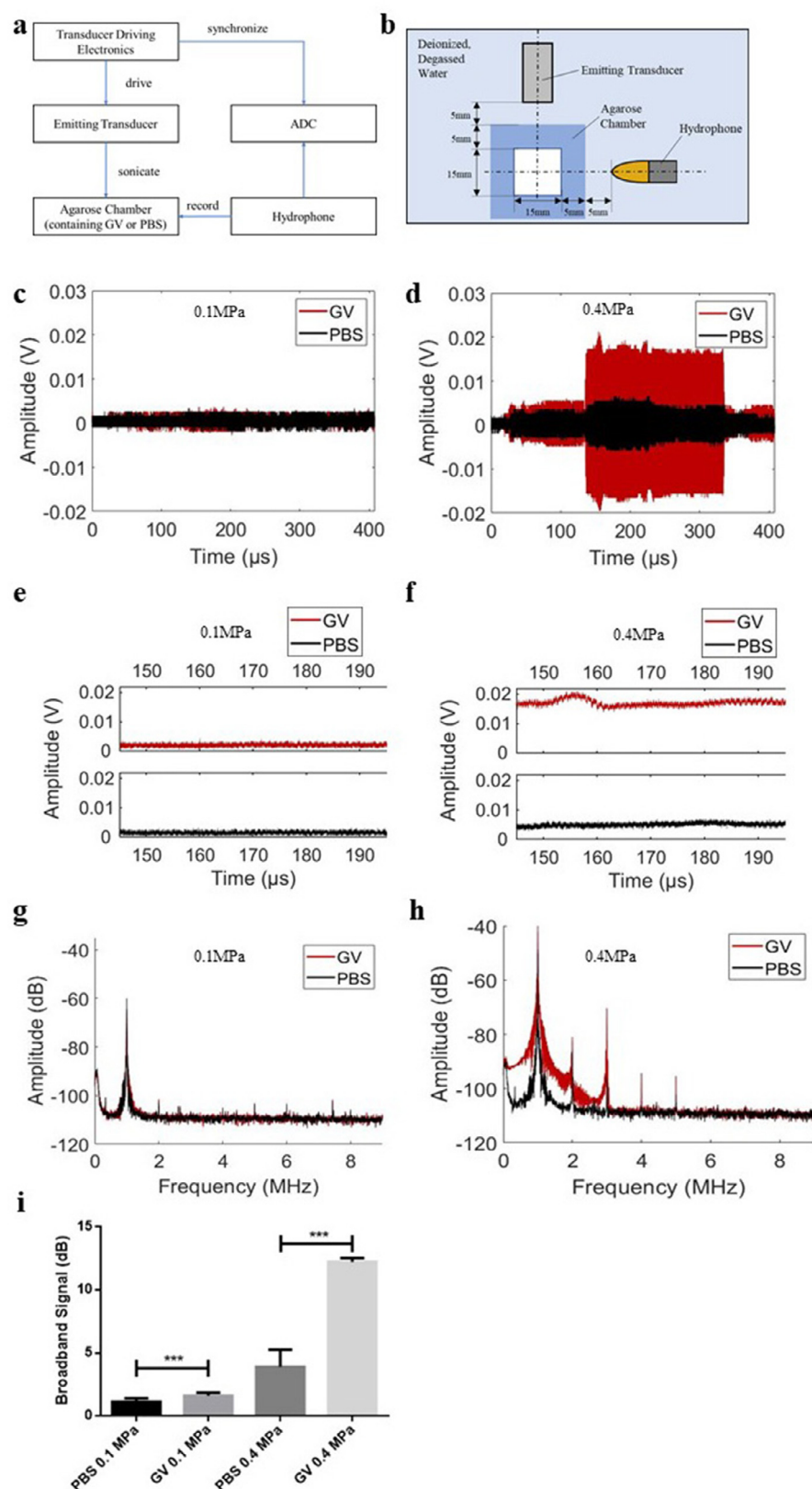
Fig. 3. GV-mediated cavitation detection. (a) Block diagram of setup for detection of GV-mediated cavitation. (b) Setup for detection of GV-mediated cavitation in solution depicted as a top view of the experimental platform. (c, d) Captured ultrasonic signal of cavitation in time-domain for GVs and PBS under (c) 0.1 MPa PRP and (d) 0.4 MPa PRP. (e,f) Temporally zoomed-in plot of the analytic envelope of the captured ultrasonic signal of cavitation in time-domain for GVs and PBS, under (e) 0.1 MPa PRP and (f) 0.4 MPa PRP. (g,h) Captured ultrasonic signal of cavitation in frequency-domain for GVs and PBS under (g) 0.1 MPa PRP and (h) 0.4 MPa PRP. (i) Quantified broadband signal (0 – 3.5 MHz) for GVs and PBS. Data represent the mean ± SD of 36 bursts from 9 independent repeats. ***$p < 0.001$.
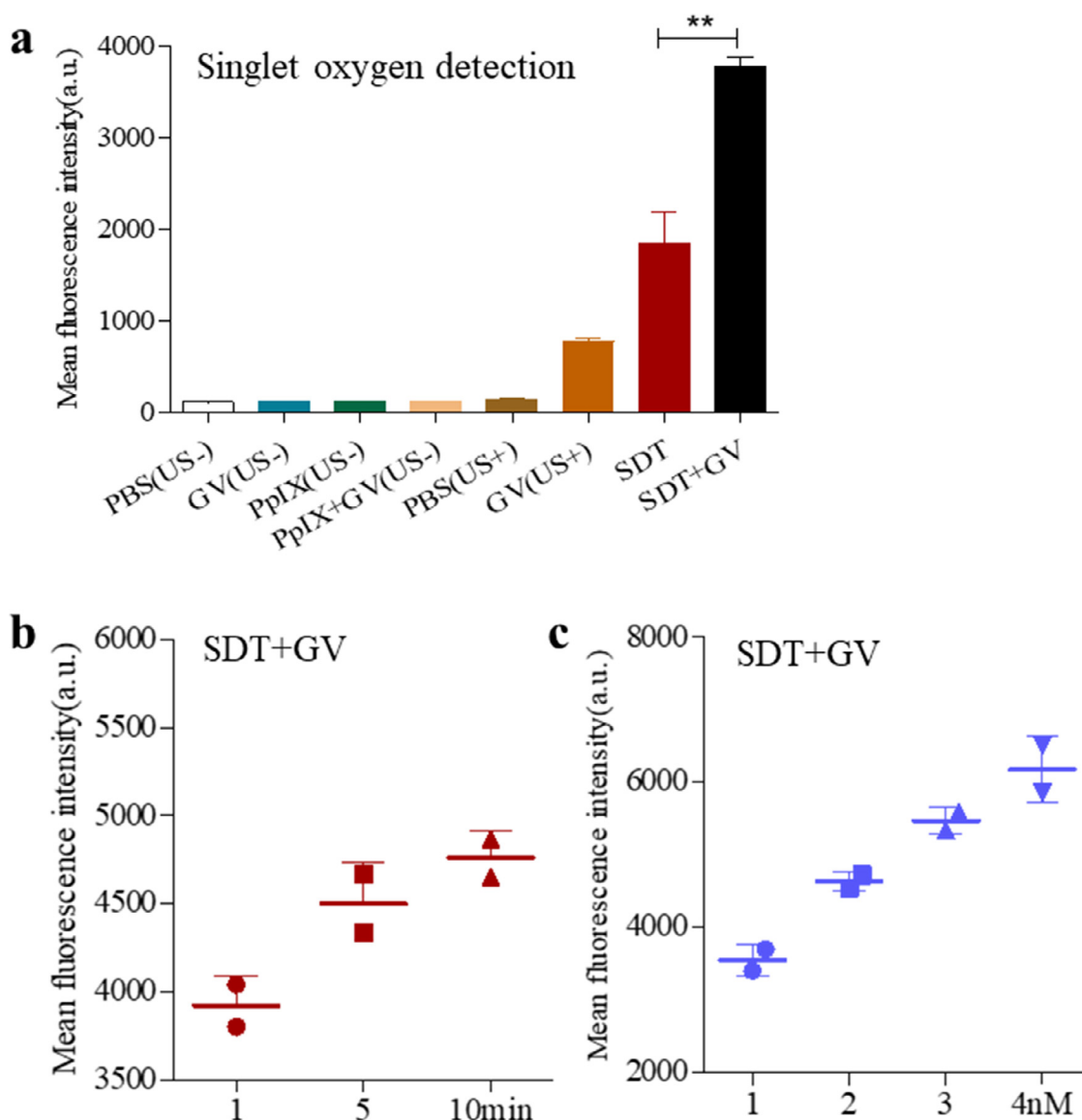
Fig. 4. GV-mediated ROS production in solution. (a) PBS, GVs (2 nM), PpIX (1 µM), and PpIX+GVs groups were treated with/without US irradiation for 5 min, and singlet oxygen production was then determined using SOSG with a fluorescent microplate reader. Bars represent the mean from three independent experiments. $^{**}p < 0.01$. (b) Change in SOSG fluorescence intensity in SDT+GVs group as a result of increased ultrasound exposure time. Data are represented as mean $\pm$ SD ($n = 3$). (c) Change in SOSG fluorescence intensity in SDT+GVs group with increasing GVs concentration. Data are represented as mean $\pm$ SD ($n = 3$).

3.5. GVs mediated cell viability and apoptosis detection

Next, the efficacy of FGVs on the cytotoxicity of *in vitro* SDT on SCC-7 cells was explored. Cells were incubated with PBS,1 µM PpIX or/and 2 nM FGVs followed by US irradiation. The cell viability of SCC-7 cells was determined using a CCK-8 assay. The FGVs (US+) and SDT groups each showed some decline in cell viability, but the SDT+FGVs group showed the lowest cell viability, significantly lower than that of the SDT-alone group (Fig. 6a). No decline in cell viability was evident among those groups without sonication. The enhancement of cytotoxicity of *in vitro* SDT by GVs was further confirmed by evaluating apoptosis 4 h following SDT treatment. Over 90% of cells were found to be non-apoptotic in the unsonicated groups as well as the PBS(US+) and GVs(US+) groups; while this number decreased to $\sim$ 75% in the SDT group, it was significantly lower in the SDT+FGVs (65.4%) group under ultrasound treatment (Fig. 6b,c). The levels of late apoptosis and necrosis observed in this group were also found to be much higher than in all other groups. We conducted an additional experiment to demonstrate the function of FGVs combined with different concentrations of PpIX during SDT. A relatively low concentration of 0.5 µM and a relatively higher concentration of 2.0 µM were used for singlet production detection in the solution, ROS production *in vitro,* and cell viability assay *in vitro during* SDT. To determine whether there was different ROS production between the 0.5 µM PpIX group and 2.0 µM PpIX group, fluorescent probe SOSG (10 µM) was used to detect the production of singlet oxygen in a cell-free system among those different groups. As shown in Fig. S1a, there were minimal fluorescent signals without ultrasound, but large increases in SOSG fluorescence were observed upon sonication in the SDT group, and SDT+GVs group, with 2.0 µM PpIX group showed a significant higher ROS production in the solution. Meanwhile, ROS production *in vitro* was also determined among the 0.5 µM PpIX group and 2.0 µM PpIX group (Fig. S1b,c). Consistently, minimal fluorescent signals were observed under the microscope, but a large quantity of fluorescence was observed upon sonication in the SDT group, and SDT+GVs group, with 2.0 µM PpIX group showed a significant higher ROS production than 0.5 µM PpIX group. For cell vi-
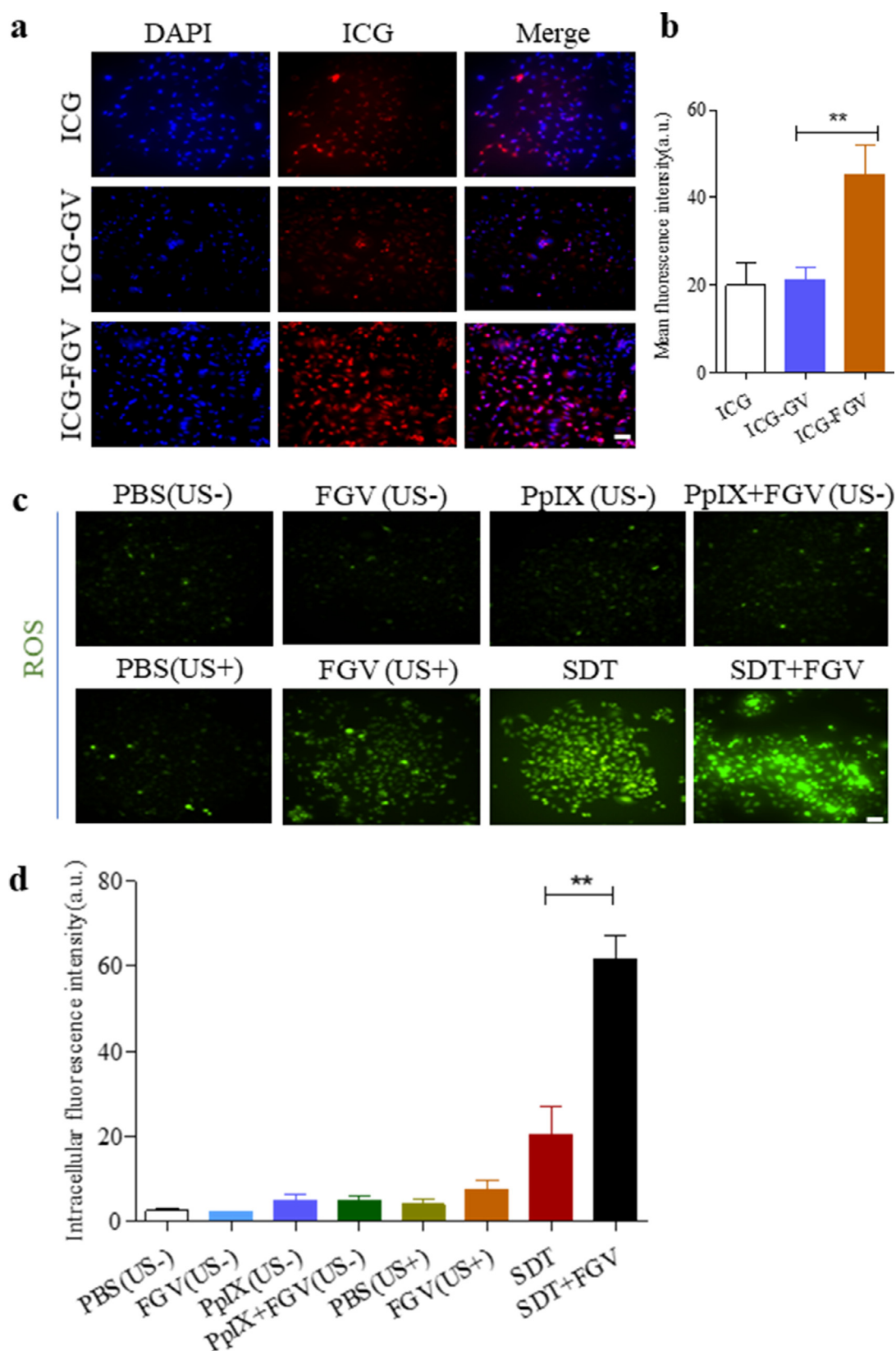
Fig. 5. ROS production mediated by functionalized GVs *in vitro*. ICG, ICG-GVs, and ICG-FGVs were co-incubated with SCC-7 cells for 4 h, confocal microscopy images were taken and representative images were shown in (a-b) with $n = 3$, Scale bar represents 20 µm. (b,c) Cells were incubated with PBS, GVs (2 nM), PpIX (1 µM), or PpIX+GVs followed by US irradiation (with/without) for 5 min. Intracellular ROS production was then determined 4 h after US treatment. Representative images of ROS generation, indicated by DCF fluorescence, as measured by fluorescent microscopy are shown($n = 3$).
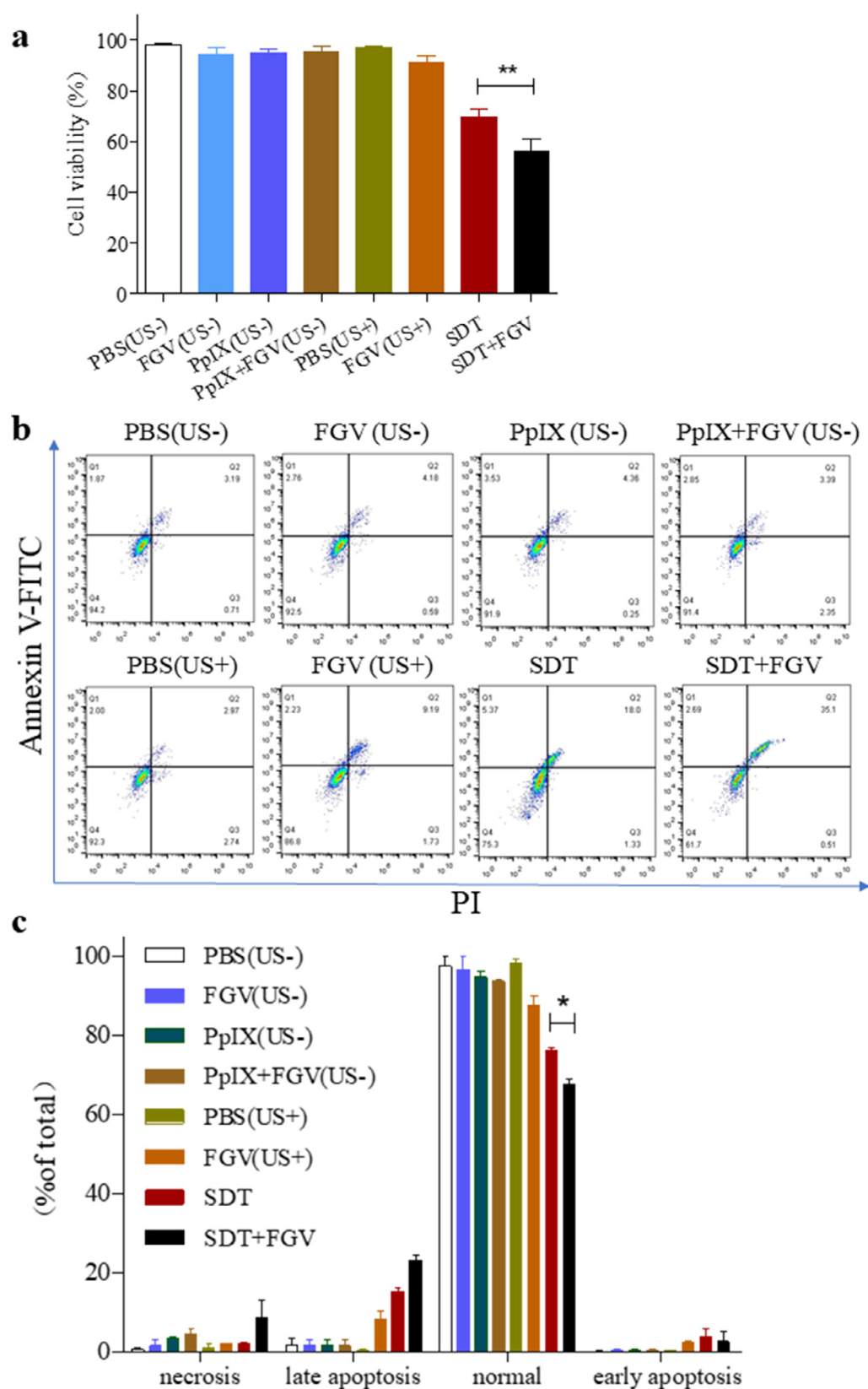
Fig. 6. *In vitro* cell viability and apoptosis assays of SDT mediated by functionalized GVs. Cells were treated with PBS, GVs (2 nM), PpIX (1 μM), or PpIX+GVs followed by US irradiation (with/without) for 5 min. Cell viability and apoptosis were determined 4 h after US treatment. (a) The relative cell viability of SCC-7 cells after different treatments was determined by a CCK-8 assay. Data represent the mean ± SD from 3 independent experiments. **$p < 0.01$. (b,c) Evaluation of cell apoptosis following different treatments was done by flow cytometry through Annexin-V and propidium iodide (PI) double staining. Data represent mean ± SD from 3 independent experiments. *$p < 0.05$.

ability assay, cell viability decreased both in SDT and SDT+FGV groups, with 2.0 μM PpIX group showed the lowest cell viability (Fig. S1d). We could conclude that the efficacy of the treatment increased as PpIX concentration increased. Generally speaking, cellular toxicity increased with higher PpIX concentration could induce higher treatment efficacy. Thus, we found that the existence of FGVs could induce significantly higher cell death and apoptosis than SDT-alone, leading to higher therapeutic efficacy for CD44$^+$ tumor cells.

3.6. In vivo *SDT assay*

We evaluated the effect of FGVs on PpIX-mediated SDT *in vivo*. FGVs (200 μl, 20 nM) were injected intratumorally(*i.t.*) into the tumor core 1 h before ultrasound irradiation to facilitate spatial retention of GVs and to see more clearly the role GVs might play in SDT. As shown in Fig. 7c, Rapid and continuous growth of tumors was observed in PBS (US-), PBS (US+), and GVs (US+) group for the following 15 days, with tumor volume reaching nearly 1000 mm^3. Both SDT and SDT+FGVs (*i.t.*) exhibited effective growth inhibition efficacy, as tumors were found to shrink significantly in the three days following SDT treatment and to regrow slowly at a slower rate. Crucially, the SDT+FGVs (*i.t.*) showed significantly smaller tumors and slower growth rate than the SDT group, demonstrating the ability of GVs to successfully enhance SDT efficacy *in vivo*.

We further determined whether intravenously injected GVs could enhance SDT. Our previous *in vivo* biodistribution results showed that large amounts of FGVs could accumulate specifically at the tumor site up to 48 h post intravenously administration and the amount peaked at 12 h [32]. Real-time NIRF imaging of mice at 12 h post-administration showed accumulation of FGVs in the tumor site after intravenous injection (Fig. 7a,b). The results in Fig. 7c showed that intravenously(*i.v.*) injected FGVs could certainly enhance SDT efficacy but the intratumoral injection was more effective. We believe the difference in effect is due to the difference of GVs' final concentration at the tumor site, as tail-vein injection involves significant GV clearance by the liver while in circulation.

No major changes in the body weights of mice in different groups were observed throughout the experimental period (Fig. 7d), indicating low systematic toxicity. The tumors were then excised and stained with H&E or a TUNEL assay to directly observe the effects of the SDT treatment. Compared to the control group, which showed normal morphology, H&E staining in both SDT and SDT+FGVs groups revealed severe damage, with the latter showing the most significant toxicity effects (Fig. 7e). Similarly, a TUNEL assay revealed much higher levels of apoptosis in SDT+FGVs than in the SDT group, with almost no apoptosis in PBS(US-), PBS(US+), and GVs(US+) groups (Fig. 7f,g). Taken together, these results demonstrate the potential of functionalized GVs to enhance SDT outcomes *in vivo*, particularly their capacity to target the tumor site specially and induce tumor toxicity.

3.7. In vitro *and* in vivo *toxicity detection*

Finally, we tested the toxicity of GVs and FGVs alone to examine their biocompatibility. MTT and apoptosis assays were used for this purpose *in vitro*. We treated cells with different concentrations of GVs/FGVs for 24 or 48 h. Cells showed that no significant changes in viability were found at any time point for both GVs' groups compared to the control (Fig. 8a,b). Also, the addition of GVs/FGVs has no significant effects on cell apoptosis and necrosis as shown in Fig. 8c,d. We then examined the major organs (heart, liver, spleen, lungs, and kidneys) of mice one week after GVs/FGVs' administration. Hematoxylin and eosin (H&E) staining of tissue slices from both GVs' and FGVs' groups presented no significant pathological abnormalities or lesions compared to the control group (Fig. 8e).

We thus determined that both GVs and FGVs alone have negligible toxicity to cells and did not cause any significant damage *in vivo*.

4. Discussion

In the present study, we lay out a role for GV-based nanoplatforms for enhanced targeted sonodynamic therapy of cancer cells. Our results showed that large quantities of ROS could be generated during SDT, inducing cell death and apoptosis both *in vitro* and *in vivo*. Specifically, we consistently found that a larger quantity of ROS was generated both in solution and in *vitro* with the addition of GVs during SDT. Singlet oxygen production in the SDT group as ultrasonic exposure time increased over time but did not elevate significantly after 5 min. This means that most of the GVs were used up within 5 min. Obvious increases in cell death and apoptosis were observed with the addition of GVs compared to SDT alone. Beside, cellular toxicity increased with higher PpIX concentration, higher GV concentration, and higher ultrasound pressure could induce higher treatment efficacy. Thus, a higher apoptosis rate could be attained by optimization of the parameters including PpIX concentration, GV concentration, as well as ultrasound parameters. GVs were observed to enhance the damage induced by SDT to tumors, as well as inhibit tumor regrowth. We also augmented the treatment by using functionalized GVs with ultrasound to enable more selective SDT treatment. This allowed targeted disruption of selected (CD44$^+$) cells in the area sonicated. In addition, no ROS production, cellular apoptosis, or cell death was observed with GVs alone, nor were other major indications of treatment-induced systemic toxicity observed. These results show GVs to be well-tolerated compared to other organic or inorganic materials, consistent with our previous studies [25,32]. We noted that the biodistribution of FGV after intravenous injection *in vivo* from IVIS results showed obvious fluorescence at the liver believed to be the clearance process to 8 h and sometimes even to 24 h due to individual variations [32]. Detail pharmacokinetic accumulation of FGVs including major organs' metabolism needs detailed confirmation in the further *in vivo* study. In conclusion, GVs consistently increased the efficacy of SDT *in vitro* and *in vivo* by significantly increasing the ROS production and become a promising nanoplatform for more targeted therapeutic efficacy under ultrasound irradiation.

The previous study also demonstrated some nanoparticles (NPs) such as gold NPs, silicon NPs or Titania NPs could function as cavitation nuclei and promoting the therapeutical efficacy under US treatment [37,38]. Beside, higher toxicity could be attained by functionalized with chemical groups or combined with stimuli of both ultrasound and light [37,38]. Compared to these NPs, the ability of GVs to serve as therapeutic enhancers in addition to their well-established role as ultrasound contrast agents also makes their application as theranostic particles possible even for further-improved treatments such as ultrasound imaging-guided targeted cancer therapy.

While our results are encouraging, further study is needed to achieve greater spatial and molecular specificity. In particular, research is required to study the influence of functionalized GVs' physical and chemical properties on therapeutic efficiency and their ability to target desired cells during SDT. Ultrasonic parameters such as intensity, mechanical index, and duty cycle may all have effects on GVs' effects and could be tuned to increase or even optimize treatment efficacy. Additional engineering of GVs may also be needed to achieve better cellular targeting, such as using more tumor-specific cell surface markers, or a combination of cell-surface molecules to better tailor the enhanced SDT treatment. Such modifications in the treatment scheme would require deep systematic study but could enable SDT treatments that are more targeted and more effective in the future.
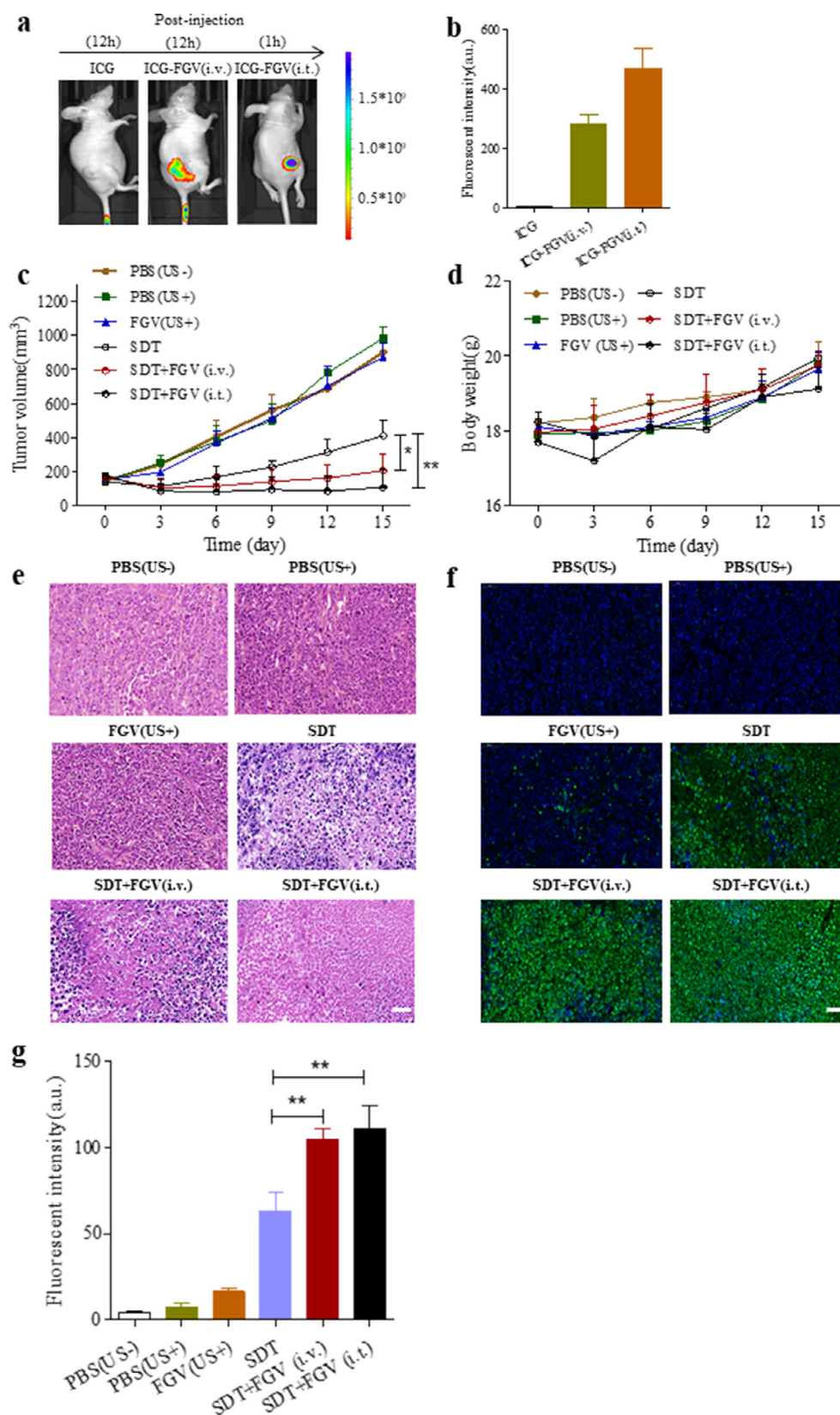
Fig. 7. Enhanced SDT mediated by functionalized GVs *in vivo*. (a) *In vivo* NIR fluorescent imaging of tumor-bearing mice, taken post-administration of free ICG (200 μl, 20 μg), and ICG-FGVs (20 nM, containing 20 μg ICG). (b) Quantitative analysis of fluorescent intensity at 12 h post-injection. Bars represent the mean ± SD from 3 independent experiments. ***$p < 0.001$ (c) Tumor growth curves of SCC-7 tumor-bearing mice with different treatments. $n = 5$ mice per group, *$p < 0.05$. **$p < 0.01$ (d) Body weights of SCC-7 tumor-bearing mice after various treatments at different time-points. (e) Representative histological images of H&E stained tumor slices were collected from different groups. Scale bar represents 50 μm. (f) Representative images of a TUNEL assay on tumor slices were collected from different groups. Scale bar represents 50 μm. (g) Quantitative analysis of the fluorescent intensity of TUNEL assay. Data represent mean ± SD from 3 independent experiments. **$p < 0.01$.
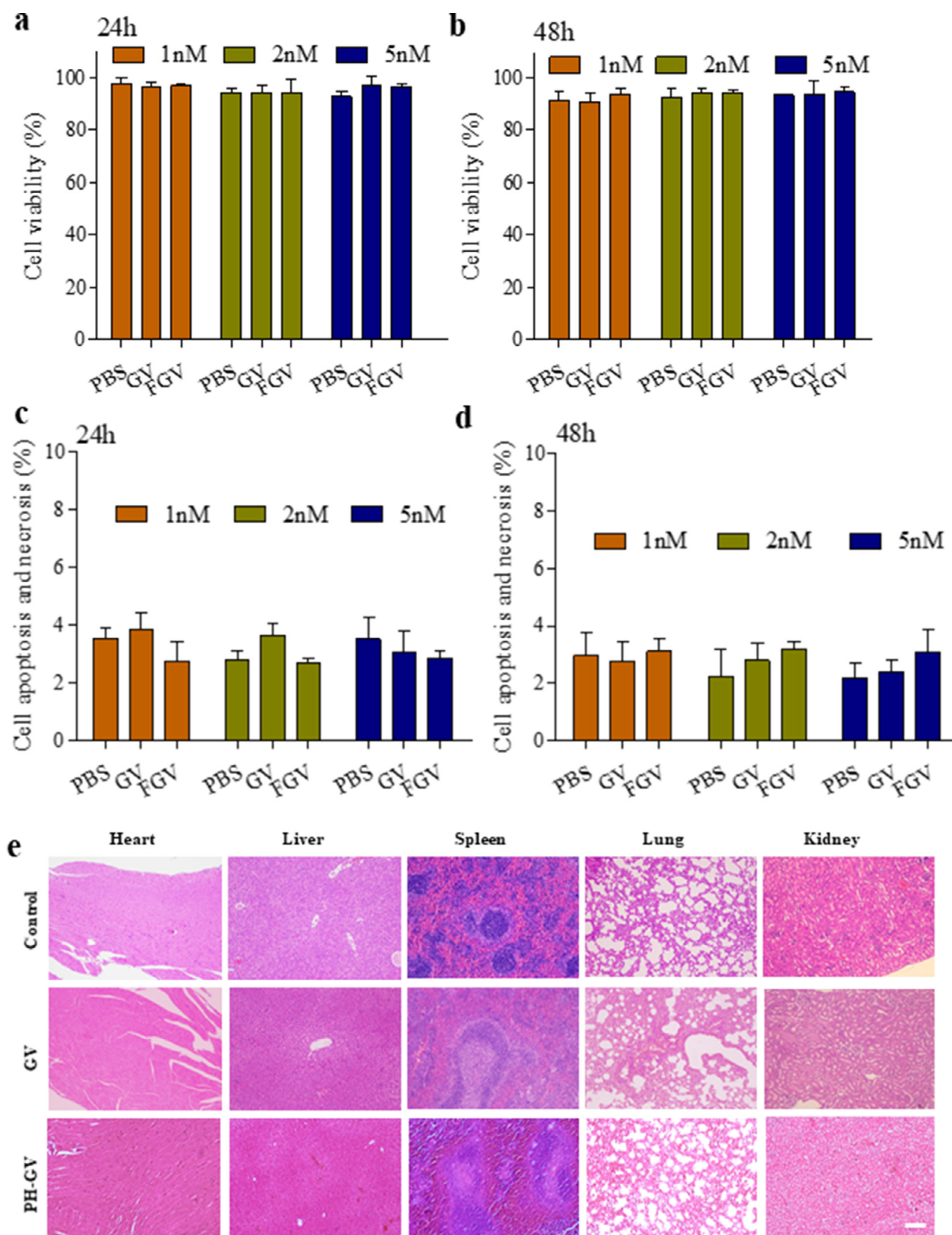
Fig. 8. Toxicity of GVs both *in vitro* and *in vivo*. Viability assay of SCC-7 cells after treatment with GVs or FGVs at the concentration of 1 nM and 5 nM, respectively, for 24 h (a) and 48 h (b). Cell apoptosis and necrosis of SCC-7 cells after treatment with GVs or FGVs at the concentration of 1 nM and 5 nM, respectively, for 24 h (c) and 48 h (d). (e) Representative H&E sections of the vital organs (heart, liver, spleen, lung, and kidney.) after GVs/FGVs treatment (200 μl of 20 nM, tail injection) on day 7. Scale bars, 100 μm.

Declaration of Competing Interest

The authors declare that they have no known competing financial interests or personal relationships that could have appeared to influence the work reported in this paper.

Acknowledgments

Supplementary materials

Supplementary material associated with this article can be found, in the online version, at doi:10.1016/j.actbio.2021.09.010.

References

[1] R. Baskar, K.A. Lee, R. Yeo, K.W. Yeoh, Cancer and radiation therapy: current advances and future directions, Int. J. Med. Sci. 9 (3) (2012) 193–199.

[2] S. Dallavalle, V. Dobricic, L. Lazzarato, E. Gazzano, M. Machuqueiro, I. Pajeva, I. Tsakovska, N. Zidar, R. Fruttero, Improvement of conventional anti-cancer drugs as new tools against multidrug resistant tumors, Drug Resist. Update 50 (2020) 100682.

[3] G. Delaney, S. Jacob, C. Featherstone, M. Barton, The role of radiotherapy in cancer treatment: estimating optimal utilization from a review of evidence-based clinical guidelines, Cancer 104 (6) (2005) 1129–1137.

[4] M.J. Lind, Principles of systemic anticancer therapy, Medicine (Baltimore) 48 (2) (2020) 90–96.

[5] G.Y. Wan, Y. Liu, B.W. Chen, Y.Y. Liu, Y.S. Wang, N. Zhang, Recent advances of sonodynamic therapy in cancer treatment, Cancer Biol. Med. 13 (3) (2016) 325–338.

[6] M. Lafond, S. Yoshizawa, S.I. Umemura, Sonodynamic Therapy: advances and challenges in clinical translation, J. Ultrasound Med. 38 (3) (2019) 567–580.

[7] D. Costley, C. Mc Ewan, C. Fowley, A.P. McHale, J. Atchison, N. Nomikou, J.F. Callan, Treating cancer with sonodynamic therapy: a review, Int. J. Hyperth. 31 (2) (2015) 107–117.

[8] L. Song, Y. Huang, X. Hou, Y. Yang, S. Kala, Z. Qiu, R. Zhang, L. Sun, PINK1/Parkin-mediated mitophagy promotes resistance to sonodynamic therapy, Cell. Physiol. Biochem. 49 (5) (2018) 1825–1839.

[9] A.K. Wood, C.M. Sehgal, A review of low-intensity ultrasound for cancer therapy, Ultrasound Med. Biol. 41 (4) (2015) 905–928.

[10] X. Pan, H. Wang, S. Wang, X. Sun, L. Wang, W. Wang, H. Shen, H. Liu, Sonodynamic therapy (SDT): a novel strategy for cancer nanotheranostics, Sci. China Life Sci. 61 (4) (2018) 415–426.

[11] W. Duco, V. Grosso, D. Zaccari, A.T. Soltermann, Generation of ROS mediated by mechanical waves (ultrasound) and its possible applications, Methods 109 (2016) 141–148.

[12] L. Rengeng, Z. Qianyu, L. Yuehong, P. Zhongzhong, L. Libo, Sonodynamic therapy, a treatment developing from photodynamic therapy, Photodiagn. Photodyn. Ther. 19 (2017) 159–166.

[13] S. Son, J.H. Kim, X. Wang, C. Zhang, S.A. Yoon, J. Shin, A. Sharma, M.H. Lee, L. Cheng, J. Wu, J.S. Kim, Multifunctional sonosensitizers in sonodynamic cancer therapy, Chem. Soc. Rev. 49 (2020) 3244–3261.

[14] H. Wang, P. Wang, L. Li, K. Zhang, X. Wang, Q. Liu, Microbubbles enhance the antitumor effects of sinoporphyrin sodium mediated sonodynamic therapy both *in vitro* and *in vivo*, Int. J. Biol. Sci. 11 (12) (2015) 1401–1409.

[15] E. Beguin, S. Shrivastava, N.V. Dezhkunov, A.P. McHale, J.F. Callan, E. Stride, Direct evidence of multibubble sonoluminescence using therapeutic ultrasound and microbubbles, ACS Appl. Mater. Interfaces 11 (22) (2019) 19913–19919.

[16] Y. Lin, L. Lin, M. Cheng, L. Jin, L. Du, T. Han, L. Xu, A.C.H. Yu, P. Qin, Effect of acoustic parameters on the cavitation behavior of SonoVue microbubbles induced by pulsed ultrasound, Ultrason. Sonochem. 35 (2017) 176–184 Pt A.

[17] K.B. Bader, E. Vlaisavljevich, A.D. Maxwell, For whom the bubble grows: physical principles of bubble nucleation and dynamics in histotripsy ultrasound therapy, Ultrasound Med. Biol. 45 (5) (2019) 1056–1080.

[18] A. Gnanaskandan, C.T. Hsiao, G. Chahine, Modeling of microbubble-enhanced high-intensity focused ultrasound, Ultrasound Med. Biol. 45 (7) (2019) 1743–1761.

[19] Y. Wang, X. Li, Y. Zhou, P. Huang, Y. Xu, Preparation of nanobubbles for ultrasound imaging and intracelluar drug delivery, Int. J. Pharm 384 (1–2) (2010) 148–153.

[20] S. Zullino, M. Argenziano, I. Stura, C. Guiot, R. Cavalli, From micro- to nano–multifunctional theranostic platform: effective ultrasound imaging is not just a matter of scale, Mol. Imaging 17 (2018) 1536–1552.

[21] T. Yin, P. Wang, R. Zheng, B. Zheng, D. Cheng, X. Zhang, X. Shuai, Nanobubbles for enhanced ultrasound imaging of tumors, Int. J. Nanomed. 7 (2012) 895–904.

[22] L. Abou-Elkacem, S.V. Bachawal, J.K. Willmann, Ultrasound molecular imaging: moving toward clinical translation, Eur. J. Radiol. 84 (9) (2015) 1685–1693.

[23] D.I. Piraner, A. Farhadi, H.C. Davis, D. Wu, D. Maresca, J.O. Szablowski, M.G. Shapiro, Going deeper: biomolecular tools for acoustic and magnetic imaging and control of cellular function, Biochemistry 56 (39) (2017) 5202–5209.

[24] M.G. Shapiro, P.W. Goodwill, A. Neogy, M. Yin, F.S. Foster, D.V. Schaffer, S.M. Conolly, Biogenic gas nanostructures as ultrasonic molecular reporters, Nat. Nanotechnol. 9 (4) (2014) 311–316.

[25] L. Song, G. Wang, X. Hou, S. Kala, Z. Qiu, K.F. Wong, F. Cao, L. Sun, Biogenic nanobubbles for effective oxygen delivery and enhanced photodynamic therapy of cancer, Acta Biomater. 108 (2020) 313–325.

[26] J.O. Szablowski, M.G. Shapiro, Achieving spatial and molecular specificity with ultrasound-targeted biomolecular nanotherapeutics, Acc. Chem Res. 52 (9) (2019) 2427–2434.

[27] Y. Yang, Z. Qiu, X. Hou, L. Sun, Ultrasonic characteristics and cellular properties of anabaena gas vesicles, Ultrasound Med. Biol. 43 (12) (2017) 2862–2870.

[28] A. Bar-Zion, A. Nourmahnad, D.R. Mittelstein, S. Yoo, D. Malounda, M. Abedi, A. Lee-Gosselin, D. Maresca, M.G. Shapiro, Acoustically detonated biomolecules for genetically encodable inertial cavitation, (2019).

[29] R.W. Bourdeau, A. Lee-Gosselin, A. Lakshmanan, A. Farhadi, S.R. Kumar, S.P. Nety, M.G. Shapiro, Acoustic reporter genes for noninvasive imaging of microorganisms in mammalian hosts, Nature 553 (7686) (2018) 86–90.

[30] F. Pfeifer, Distribution, formation and regulation of gas vesicles, Nat. Rev. Microbiol. 10 (10) (2012) 705–715.

[31] F. Pfeifer, Haloarchaea and the formation of gas vesicles, Life (Basel) 5 (1) (2015) 385–402.

[32] G. Wang, L. Song, X. Hou, S. Kala, K.F. Wong, L. Tang, Y. Dai, L. Sun, Surface–modified GVs as nanosized contrast agents for molecular ultrasound imaging of tumor, Biomaterials 236 (2020) 119803.

[33] K.Y. Choi, K.H. Min, H.Y. Yoon, K. Kim, J.H. Park, I.C. Kwon, K. Choi, S.Y. Jeong, PEGylation of hyaluronic acid nanoparticles improves tumor targetability *in vivo*, Biomaterials 32 (7) (2011) 1880–1889.

[34] L.J. Cruz, P.J. Tacken, R. Fokkink, C.G. Figdor, The influence of PEG chain length and targeting moiety on antibody-mediated delivery of nanoparticle vaccines to human dendritic cells, Biomaterials 32 (28) (2011) 6791–6803.

[35] A.N. Koo, H.J. Lee, S.E. Kim, J.H. Chang, C. Park, C. Kim, J.H. Park, S.C. Lee, Disulfide-cross-linked PEG-poly(amino acid)s copolymer micelles for glutathione–mediated intracellular drug delivery, Chem. Commun. (Camb.) 48 (2008) 6570–6572.

[36] K.H. Min, J.H. Kim, S.M. Bae, H. Shin, M.S. Kim, S. Park, H. Lee, R.W. Park, I.S. Kim, K. Kim, I.C. Kwon, S.Y. Jeong, D.S. Lee, Tumoral acidic pH-responsive MPEG-poly(beta-amino ester) polymeric micelles for cancer targeting therapy, J. Control. Release 144 (2) (2010) 259–266.

[37] O.K. Kosheleva, T.C. Lai, N.G. Chen, M. Hsiao, C.H. Chen, Selective killing of cancer cells by nanoparticle-assisted ultrasound, J. Nanobiotechnol. 14 (1) (2016) 46.

[38] G. Canavese, A. Ancona, L. Racca, M. Canta, B. Dumontel, F. Barbaresco, T. Limongi, V. Cauda, Nanoparticle-assisted ultrasound: a special focus on sonodynamic therapy against cancer, Chem. Eng. J. 340 (2018) 155–172.